The role of the substrate on the mechanical and thermal stability of Pd thin films during hydrogen (de)sorption

Verma, Neha; Delhez, Rob; van der Pers, Niek M.; Tichelaar, Frans D.; Böttger, Amarante J.

DOI
10.1016/j.ijhydene.2020.10.163

Publication date
2021

Document Version
Final published version

Published in
International Journal of Hydrogen Energy

INTERNATIONAL JOURNAL OF HYDROGEN ENERGY 46 (2021) 4137–4153

Available online at www.sciencedirect.com

ScienceDirect

journal homepage: www.elsevier.com/locate/he

The role of the substrate on the mechanical and thermal stability of Pd thin films during hydrogen (de)sorption

Neha Verma [a,*], *Rob Delhez* [a], *Niek M. van der Pers* [a], *Frans D. Tichelaar* [b], *Amarante J. Böttger* [a]

[a] *Department of Materials Science and Engineering, Delft University of Technology, Mekelweg 2, 2628, Delft, CD, the Netherlands*

[b] *Kavli Institute of NanoScience, Delft University of Technology, Lorentzweg 1, 2628, Delft, CJ, the Netherlands*

HIGHLIGHTS

- Pd thin film–morphology and substrate interaction studied.
- Open columnar morphology inhibits H-induced buckling delamination.
- Pd film on a flexible PI interlayer exhibits free-standing film-like behavior.
- All Pd films contain similar kinds of defects but differ by defect density.
- The softer interface corresponds to the stronger thin film system.

ARTICLE INFO

Article history:
Received 10 July 2020
Received in revised form
10 October 2020
Accepted 19 October 2020
Available online 10 November 2020

Keywords:
Pd thin film
Intermediate layer
Phase transitions
Microstructure
X-ray diffractions
Deformations

ABSTRACT

In this work, we studied the mechanical and thermal stability of ~100 nm Pd thin films magnetron sputter deposited on a bare oxidized Si(100) wafer, a sputtered Titanium (Ti) intermediate layer, and a spin-coated Polyimide (PI) intermediate layer. The dependence of the film stability on the film morphology and the film-substrate interaction was investigated. It was shown that a columnar morphology with elongated voids at part of the grain boundaries is resistant to embrittlement induced by the hydride formation ($\alpha \leftrightarrow \beta$ phase transitions). For compact film morphology, depending on the rigidity of the intermediate layer and the adherence to the substrate, complete transformation (Pd-PI-SiO_2/Si) or partly suppression (Pd-Ti-SiO_2/Si) of the α to β-phase was observed. In the case of Pd without intermediate layer (Pd-SiO_2/Si), buckling delamination occurred. The damage and deformation mechanisms could be understood by the analysis of the stresses and dislocation (defects) behavior near grain boundaries and the film-substrate interface. From diffraction line-broadening combined with microscopy analysis, we showed that in Pd thin films, stresses relax at critical stress values via different relaxation pathways depending on film-

* *Corresponding author*. Department of Materials Science and Engineering, Delft University of Technology, Mekelweg 2, 2628, Delft, CD, the Netherlands.

E-mail addresses: N.Verma@tudelft.nl, chem.neha@gmail.com (N. Verma), R.Delhez@tudelft.nl (R. Delhez), N.M.vanderPers@tudelft.nl (N.M. van der Pers), F.D.Tichelaar@tudelft.nl (F.D. Tichelaar), A.J.Bottger@tudelft.nl (A.J. Böttger).

https://doi.org/10.1016/j.ijhydene.2020.10.163

microstructure and film-substrate interaction. On the basis of the in-situ hydriding experiments, it was concluded that a Pd film on a flexible PI intermediate layer exhibits free-standing film-like behavior besides being strongly clamped on a stiff SiO_2/Si substrate.

Introduction

In recent years, substantial amounts of research were performed on Palladium (Pd) in view of a future hydrogen economy [1–5]. Since Pd readily absorbs hydrogen even at low pressure and room temperature [6,7], Pd and its alloys [8] are suitable for hydrogen purification [9], hydrogen storage [10], hydrogen gas sensors [11], and fuel cell catalysts [12]. However, primary requirements for the application are not always satisfied, such as usability under operation conditions (temperature and pressure), minimum investment cost, and sustain hydrogen embrittlement [13–17].

Hydrogen absorption properties in metals depend on the microstructure and have been studied from this point of view for several metal-hydrogen (M–H)-systems [18]. The various microstructures offer different types of hydrogen trapping sites, in bulk and as well as in nanostructured thin films. Nanostructured Pd has shown high hydrogen diffusivity due to grain boundaries that act as a network of fast diffusion pathways [19,20]. Nanosizing also dramatically alters material properties, which are strongly affected by the presence of crystallographic defects. Ulvestad et al. [21] and Narayan et al. [22] demonstrated that the ability of the defective Pd nanoparticle to remove crystallographic imperfections is the reason for nano-sized system's durability under the stresses resulting from large volume changes during hydrogen absorption and desorption. They also showed that these structural defects act as additional barriers to the phase transformation. Similar observations were made in nanocrystalline Pd films [23].

In thin films, large mechanical stresses are induced when loaded with hydrogen as caused by an elastic constrain from the substrate [24,25], known as substrate clamping. When the in-plane expansion is suppressed by adhesion to the substrate, high compressive in-plane stresses are built [26,27]. These high internal stresses are the cause of buckling [28] and local or complete detachment of the film from the substrate at a certain critical concentration of absorbed hydrogen [29,30]. Larger hysteresis occurred upon hydrogen loading/deloading cycles in clamped than in free-standing films [28,31]. The buckling of the hydrogen-loaded thin film itself significantly increases the dislocation activity (plastic deformations) [32]. Considering the state of the literature described, we compared differences in the microstructural behavior as induced by hydrogen (de)sorption of various Pd thin films with and without an adhesive intermediate layer. Direct observation of stresses and dislocation mediated deformations were estimated using X-ray diffractometry (XRD) during *in-situ* hydriding experiments.

A study based on positron annihilation spectroscopy showed that plastic deformation leads to an increase of the defect density upon hydrogenation in various Pd films [33]. Amin-Ahmadi et al. [23] discussed the dislocation/hydrogen interaction mechanisms in hydrided nanocrystalline Pd films and showed that local plasticity in β-phase could be controlled by dislocation activity. Similar to the stress, the defects (dislocations) in thin films also led to a slower hydrogen uptake [34]. At a given deformation level, dislocations propagate and interact with pre-existing structures and also with each other, thus, makes up the final microstructure of the deformed state [18]. Stress relaxation in Pd thin film after phase transitions can be explained by the process in which change in dislocation structure plays a dominant role.

Pd thin films have limited structural stability when exposed to hydrogen gas even at room temperature, owing to the $\alpha \leftrightarrow \beta$ phase transitions [33,35,36]. The nature of the substrate, the adhesion to the substrate and the microstructure of the film are all of importance for stability [37]. It was shown that tuning the microstructure through magnetron sputtering [38], and adapting the adhesion [39] and state of stress adjusted by the nature of the underlying substrate [40] enables improvement of the film stability.

In this paper, a comprehensive *in-situ* XRD experimental study is presented to demonstrate the role of the film microstructure and intermediate layer material on the mechanical stability of Pd thin films exposed to hydrogen. The influence of film-substrate adhesion and deposition parameters of the film is found to have a profound effect both on the response of hydrogen uptake and mode of damage. It is shown that annealing significantly impacts Pd thin film performance and stability. These findings were further supported by the observation that stress relaxation mechanisms are different for Pd films with a comparable microstructure but deposited with different adhesive intermediate layer on a stiff substrate. The films have been characterized by XRD to obtain macrostress, texture and defect parameters through line-broadening analysis using integral breadth [41,42]. Transmission and scanning electron microscopy (TEM and SEM) are applied to investigate morphological changes.

Experimental

Pd thin film preparation

Two series of Palladium thin films were dc magnetron sputter deposited in an ATC 1500F sputter deposition system from AJA International. Series-1 films were deposited for 480 s at low Ar pressure of 0.4 Pa, with an average deposition rate of 0.2 nm/s. Series-2 films were deposited for 900 s at high Ar pressure of

3 Pa, with an average deposition rate of 0.1 nm/s. The base pressure of the deposition chamber was 1.3×10^{-5} Pa and argon was used as a sputtering gas. As a substrate, thermally oxidized (~188 nm) 2-inch single-crystal Si(100) wafers (SiO_2/Si) were used with and without an intermediate layer. Two different adhesive intermediate layers were laid between Pd film and SiO_2/Si substrate: (i) a sputter-deposited 6 nm Titanium (Ti) layer (Ti-SiO_2/Si), or (ii) a spin-coated 5 μm thick polyimide (PI) layer (PI-SiO_2/Si). All depositions were performed with a substrate temperature of 293 K.

The Ti layer deposition on the SiO_2/Si wafer was performed at two working Ar pressures, 0.4 Pa (for series-1) and 3 Pa (for series-2) for 70 s and 360 s, respectively. Polyimide spin-coating on the SiO_2/Si wafer was performed at Else Kooi Lab (EKL), TU Delft. Before PI spin coating, the wafers were primer coated with VM652 primer at 3500 rpm for 10 s, to promote adhesion of PI to the wafers, followed by a 5 μm thick layer of PI Duramide 115 A spin-coated at 4000 rpm. The PI layer was soft-baked at 388 K for 15 s and subsequently cured at 673 K for 2 h.

TEM and SEM: morphology analysis

The cross-sectional morphology of the Pd thin film was characterized using CM30T and CM300UT-FEG Philips Transmission Electron Microscopy (TEM), type Tecnai F20ST/STEM (FEI Electron Microscopes) with energy dispersive spectroscopy (EDS). The investigated TEM foils were prepared by Argon-ion milling of a cross-sectional cut protected by a glass plate glued to the film. The surface morphology of the Pd thin films was examined using Scanning Electron Microscopy (SEM) - JEOL JSM 6500F, equipped with a Thermo Fisher Ultradry detector with Noran system 7 data-acquisition and data-analysis software.

X-ray diffraction (XRD)

In-situ X-ray diffraction (XRD) measurements were used to investigate hydrogen-induced changes in texture, stress and microstructure of Pd thin films during hydrogen loading/deloading (absorption and desorption). Two different diffractometers, one with parallel-beam geometry (CoKα) and one with focusing geometry (CuKα), were used.

Texture and stress measurements

The simultaneous stress/texture measurements were performed on a Bruker-AXS D8 Discover diffractometer equipped with polycapillary optics (0.25°) and Eulerian cradle in parallel beam geometry (CoKα; 45 kV, 25 mA). Data were collected over 2θ ranges that cover the whole diffraction peak at different sample orientations (ψ tilting the sample at fixed rotation angle ϕ). The rotational symmetry of the texture was confirmed by additional pole figures measurement. The integrated intensities of the {111} reflection were presented as a fiber texture plot (FTP) displaying the distribution of the texture components about the fiber axis from the center ($\psi = 0°$) to the outer edge ($\psi = 75°$). The integrated intensities after a linear background fitting were obtained using the Bruker – EVA software [43]. Measured intensities were corrected for thin layer and instrumental intensity loss [44].

The same measured scans were used to determine the in-plane stresses and data evaluation was done with the PANalytical X'Pert Stress Plus [45]. Stress states were determined using the conventional $\sin^2\psi$ method [46]. From the Pd{311} reflection, the lattice plane spacing, was determined. In this work, the Neerfeld-Hill average values [46] for the X-ray elastic constants, $S_1(311)$ and $\frac{1}{2}S_2(311)$ were taken, −3.25 and 11.49 TPa^{-1} for Pd; and −3.28 and 11.60 TPa^{-1} for $PdH_{0.66}$, respectively at 300 K, as calculated from Pd single-crystal elastic constants [47]. It should be noted that, in addition to crystallographic texture, the sputter-deposited columnar grain structure is responsible for the macroscopic anisotropy [48]. Therefore, we estimated the stress in Pd thin films based on a single-crystal type analysis [49] using only the crystallites with {111} planes parallel to the film surface. Those crystallites contribute to the {311} FTP with maxima at 29.5° and 58.5° ψ-tilt angles.

For series-1 films, the data from the maxima at 29.5° and 58.5° ψ-tilt angles were used. Since series-2 films used in this study have weak and broad {111} fiber texture, at least three ψ tilt angles were used around 29.5° and 58.5° ψ-tilt angles for the stress measurements. The stress parallel to the surface $\sigma_{//}$was calculated from the slope of the straight line fitted to the data in the plot of d_ψ^{hkl} versus $\sin^2\psi$.

XRD line-broadening: microstructure characterization

The deformation mechanisms in terms of defect parameters such as crystallite sizes and lattice strain due to dislocations were obtained by line-broadening analysis of X-ray diffraction profiles using the integral breadth [42]. These were determined by profile fitting to the measured line profiles after $K_{\alpha 2}$-stripping using the least-squares multi-peak fitting implemented in Igor Pro [50], assuming a linear background and a Voigt function line shape. This profile fitting was found to be necessary because most of the line profiles used showed a small but distinct overlap with neighboring reflections.

For line-broadening analysis, Pd- {111}, {311} and {222} HKL reflections were selected from "long scans" made on the Bruker D5005 (section Above room-temperature). The {220} reflection was not measured because of interfering Si(400) reflection from SiO_2/Si wafer substrate. Further, the {200} reflection was not used for analysis because the overlap with the {111} reflection was found to affect fitting results. The instrumental profile was determined by measuring, under analogous conditions, a reference specimen of NIST/NBS LaB_6 powder (SRM660a) [51] on a (510) Si single-crystal substrate. Standard deviations for the integral breadth (β) were estimated by measuring ten times the four HKL reflections of a Pd-SiO_2/Si specimen, then used as an estimate of the standard deviations of all measurements. This seems justified because only small differences between the β_{hkl} values for the various specimens and treatments are observed. Similarly, for the instrumental profile, seven identical scans were performed on LaB_6 and from the integral breadth values of each reflection, the average and standard deviation were calculated.

The measured XRD peak profile or measured broadening is the result of the convolution of the instrumental broadening of the diffractometer and the broadening introduced by microstructural imperfections in the sample called micro-

structural broadening [41]. The instrument-corrected broadening β_{hkl} corresponding to the diffracted peak of Pd thin film was estimated using:

$$\beta_{hkl} = \left[(\beta_{hkl})^2_{measured} - (\beta_{hkl})^2_{instrumental}\right]^{1/2} \quad (1)$$

because the shape of all line profiles involved was close to Gaussian as found from profile fitting.

In the rest of this study β^*_{hkl}, the integral breadth in reciprocal space is used instead of β_{hkl}:

$$\beta^*_{hkl} = \beta_{hkl}\cos\theta/\lambda \quad (2)$$

It is assumed here that the microstructural broadening was caused by macrostrain induced broadening arising from crystal imperfections and small crystallite size, and that the effects of broadening by these two components are additive of the total integral breadth of a Bragg peak.

There was no effect found of stacking and twin faults in the measured lattice constants [52]. Therefore the line breadths were assigned to dislocations and evaluated by the modified Williamson-Hall (mod-WH) method [53,54]. The method accounts for the anisotropic strain fields of dislocations by introducing the Contrast Factor C_{hkl}. C_{hkl} depends on the types, densities, and arrangements of the dislocations present, as well as on the orientation distribution of the dislocations with respect to the diffraction vector g_{hkl}.

$$\beta^*_{hkl} = K\Big/ < D > + \left(\pi M^2 b^2/2\right)^{1/2}\left[\left(h^2+k^2+l^2\right)\Big/a^2\right]^{1/2}\rho^{1/2}C^{1/2}_{hkl} \quad (3)$$

where K is a constant (here taken = 1), $< D >$ (nm) is the average crystallite size (here perpendicular to the Pd layers), M is a constant describing the dislocation arrangement [55] (here taken = 1), ρ is the dislocation density (m^{-2}), b is the Burgers vector, and a is the lattice constant. The contrast factors C_{hkl} are tabulated in the Supplementary material (Table S1). The contrast factors C_{hkl} were calculated (see Appendix) for untextured material containing randomly oriented screw and edge dislocations of the {111}, a/2<110> slip system and of other slip systems, using the anisotropic elastic constants for Palladium (the values used of the elastic compliances s11, s12 and s44 are 13.7444, −5.99504 and 14.0351 TPa^{-1}, respectively [46]).

Experimental set-up for in-situ *hydriding*

The hydrogen absorption and desorption in Pd thin film were observed by collecting diffraction patterns during hydrogen loading/deloading experiments performed on two different *in-situ* XRD.

Room temperature

For direct visualization of the topographic changes on Pd film surface, one hydrogen loading/deloading cycle at room-temperature (RT) was performed in a custom-made sample holder on the Bruker D8 Discover (see section Texture and stress measurements) using CoKα radiations. The sample holder consists of a cavity covered by a transparent foil (4 μm Chemplex Propylene) that enables to capture (via eyes and camera) pictures of the surface (Fig. 4(a–i)) during *in-situ* measurement under continuous gas flow. Diffraction patterns were collected over a "short-scan" in the range 43–49° 2θ (including the Pd-{111} α and β phase), under the following conditions: (i) as-deposited specimen in air, (ii) during hydrogen loading in H_2/N_2 gas ($p(H_2)$ = 0.05 atm) at 2 min interval up to complete α to β phase transition; and (iii) during hydrogen deloading in air, every 2 min until complete transition back to Pd metallic state containing "no" hydrogen.

Above room temperature

Several loading/deloading conditions were investigated *in-situ* above room-temperature using a Bruker D5005 diffractometer in Bragg-Brentano focusing geometry (CuKα; 40 kV, 30 mA), equipped with MRI HT chamber. The chamber is equipped with a mass flow controller for N_2 (1 atm) gas and H_2/N_2 ($p(H_2)$ = 0.05 atm). The chamber is at atmospheric pressure. The specimen was mounted on a Pt–Rh heater strip with a fixed S-type thermocouple. Another thermocouple K-type was placed on the specimen surface to measure the actual specimen temperature.

Phase transitions: 303 K–353 K (PT-only). For the detection of hydrogen-induced transformations in Pd film, diffraction patterns were recorded in the H_2/N_2 gas mixture in 10 K steps from 303 K–353 K. Phase transitions (PT) were tracked by measuring the Pd-{111} reflections of the α and β-phase. Diffraction patterns for monitoring PT were collected over a "short scan" in the range 36–43° 2θ with a step size of 0.04°, using a fixed slit. The net peak area was used as a measure for the phase amounts. For the analysis of the microstructure (through line-broadening), XRD patterns of the film before (as-dept.) and after phase transitions (after-PT) were collected in N_2 gas atmosphere using a "long scan" over three ranges: 35 - 43° 2θ (including the Pd-{111}), 43 - 50° 2θ (including the Pd-{200}) and 77 - 90° 2θ (including the Pd- {311} and {222} reflections). The long scans were recorded using a variable divergence slit to achieve data with a constant irradiated length for the whole 2θ range.

High-temperature annealing prior to phase transitions (HT+PT). For high-temperature (HT) stability assessment, the Pd thin film was annealed in H_2/N_2 gas mixture up to 625 K before conducting the phase transitions (PT). Diffraction patterns were recorded under the following conditions: (i) as-deposited long scan in N_2 gas (as-dept.); (ii) heating in N_2 gas until 373 K, followed by increasing the temperature in 10 K steps in the H_2/N_2 gas mixture to 473 K or 623 K, and annealing for 18 h; (iii) after annealing and cooling down to RT, a long scan in N_2 gas (after-HT); (iv) after HT step the α↔β phase transitions in the H_2/N_2 gas was examined between 303 K–353 K as explained above for PT-only; and finally (v) H_2/N_2 gas in the chamber was replaced by N_2 gas during desorption and long scan was collected (after-HT+PT).

Results and discussion

As-prepared Pd thin film microstructure

Pd thin films deposited at two sputter pressure conditions, 0.4 Pa (series-1) and 3 Pa (series-2), and three underlying substrate conditions, *i.e.*, with an intermediate layer (Ti or PI) and without an intermediate layer (bare SiO_2/Si), were investigated to examine microstructure, adhesion conditions to the substrate and consequently the film stability when exposed to hydrogen.

Morphology

Fig. 1(a–b) shows TEM cross-sectional view of as-deposited series-1 Pd-Ti-SiO_2/Si and Pd-PI-SiO_2/Si films with compact morphology. SEM plane view in Fig. 2(a) shows the smooth surface topography of series-1 film Pd on Ti layer. The smoothness of the surface and the higher packing density of the columns is because of energetic particle bombardment at low deposition pressure [56]. When the surface mobility of the sputtered Pd atoms is high, the islands formed merge while still very thin, thereby forming a continuous film without voids. For series-1 irrespective of underlying surface conditions, the Pd deposition conditions dominate to produce high density closed morphology. Thus, TEM and SEM micrographs in Fig. 1(a–b) and 2(a) are representative of the as-deposited morphology of all series-1 films.

Pd films with relatively open morphology were obtained at high deposition pressure (series-2). Fig. 1(c–e) shows TEM images of as-deposited series-2 films. For Pd-SiO_2/Si film in Fig. 1(c), most of the vertical columnar structures are extending from the bottom to the top of the film; some, however, develop from clusters of small grains at the film-substrate interface. Adjacent columns are separated by voided-boundaries. SEM topography images in Fig. 2(b–d) confirmed a low-density open morphology for series-2 films. SEM micrographs clearly show a network of diffuse black lines indicating voids of different density and structure at the grain boundaries along with a microcrack network. These voided-boundaries stem from the decrease in the surface mobility of the adatoms after a series of collisions with the sputter gas under high deposition pressure, and as well as shadowing effects [57].

The columnar microstructure of Pd films is consistent with the predictions of Thornton's structure zone model (SZM) [57].

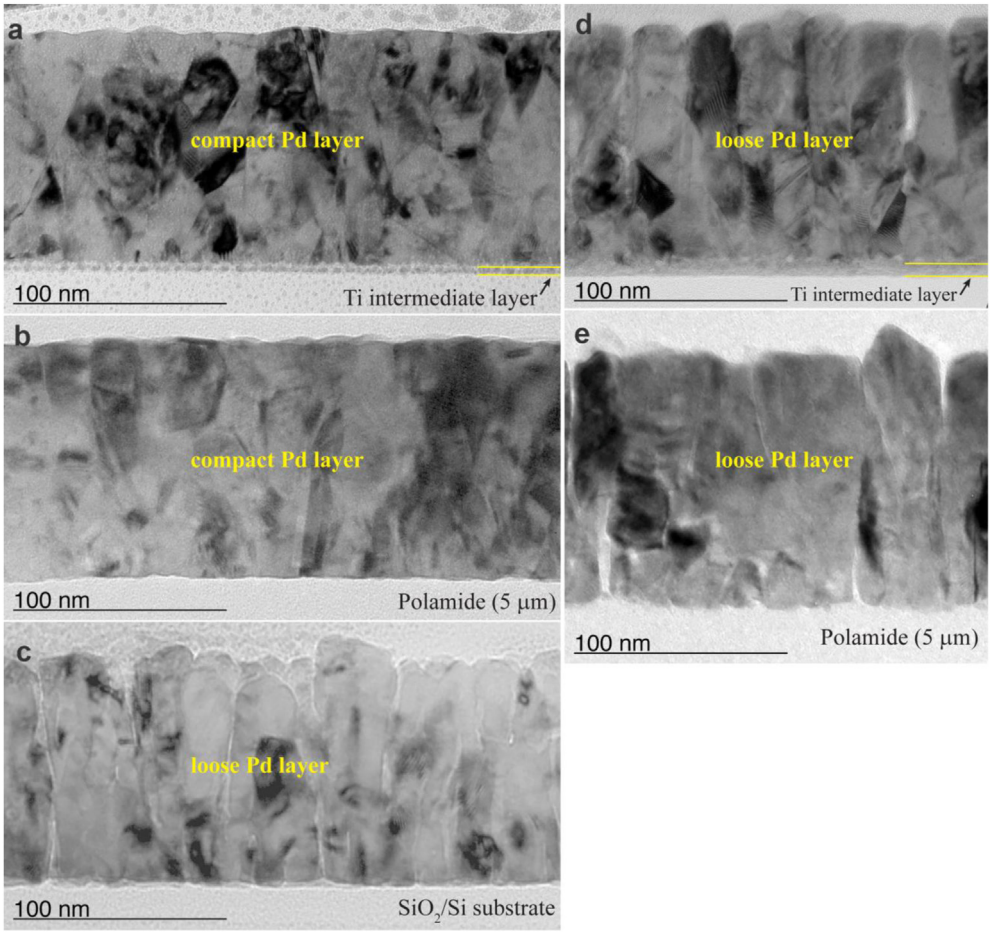

Fig. 1 – A cross-sectional view of TEM bright-field (BF) images (100 nm scale) illustrating the growth morphology of as-deposited Pd thin films. Series-1 films morphology showing non-voided compact columnar nanostructures: (a) Pd-Ti-SiO_2/Si and (b) Pd-PI-SiO_2/Si. Series-2 films with and without intermediate layer: c) Pd-SiO_2/Si, (d) Pd-Ti-SiO_2/Si and (e) Pd-PI-SiO_2/Si. All series-2 films have open columnar nanostructures with (nano)voids along the grain boundaries.

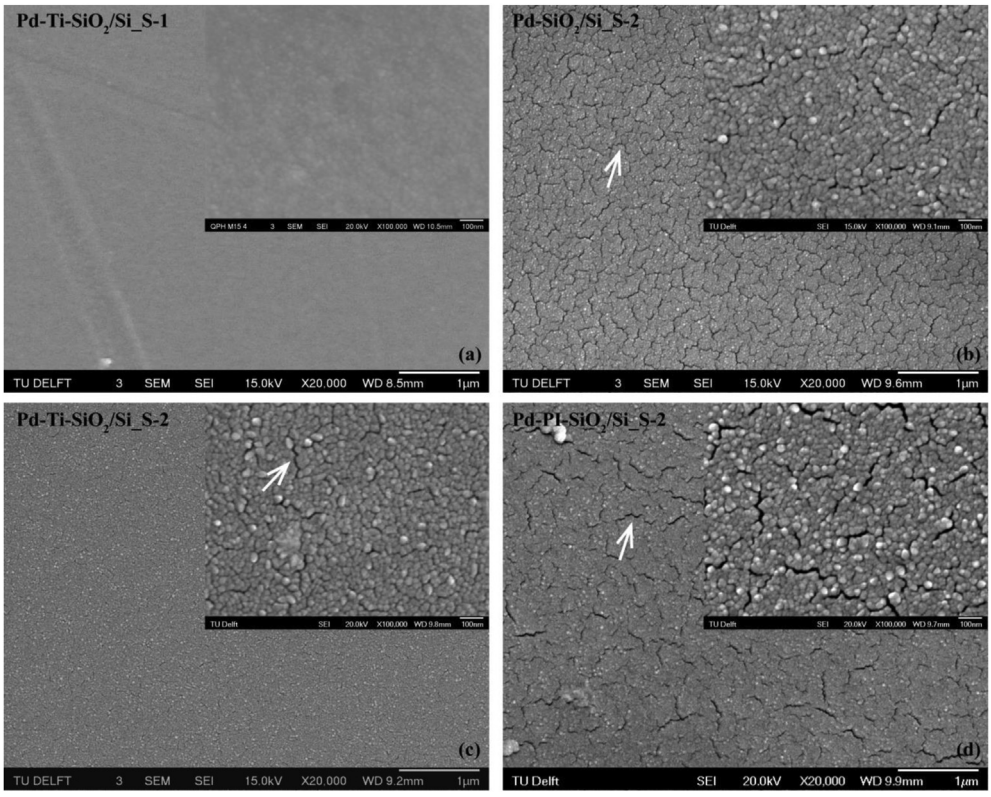

Fig. 2 – SEM images illustrating surface morphology of as-deposited Pd thin films. (a) Series-1 (S-1) film surface is showing a high-density smooth topography for Pd-Ti-SiO_2/Si. All series-2 (S-2) films showing loose/open topography: (b) Pd-SiO_2/Si, (c) Pd-Ti-SiO_2/Si and (d) Pd-PI-SiO_2/Si. The white arrows highlight the initial network of primary microcracks, which are associated with intercolumnar voids. The insets are high-magnification (100 nm) images of the Pd films.

The Pd films were deposited at a substrate temperature of 293 K, and the homologous temperature ~0.2 (Pd melting temperature 1828 K taken from Ref. [58]). Along these lines, series-1 morphology with compact columnar structures belonging to Zone T and series-2 deposited at 3 Pa Ar pressure, with open columnar structures belong to Zone 1. In previous work [40], we have shown that underlying intermediate layer roughness is also a determining factor for obtaining Pd film with an open columnar morphology. Here for series-2 film Pd on Ti layer, we used optimized Ti intermediate layer deposition parameters (thickness and deposition pressure). Pd on Ti layer in Fig. 1(d) shows a structure similar to Pd on bare SiO_2/Si substrate (Fig. 1(c)) but with less/small voids along columnar boundaries due to the relatively smooth underlying Ti-SiO_2/Si substrate.

For Pd on PI layer, Fig. 1(e) shows a rough Pd bottom, and less elongated grains are present; the columnar structure is composed of 2 or 3 grains over the thickness. The PI intermediate layer resulted in tilted Pd columns with irregularly voided-boundaries. The slow surface diffusion of adatoms and atomic shadowing results in adatom pile up on existing grains, thus favoring the formation of voided-boundaries [59]. By comparing the series-2 SEM images in Fig. 2(b–d), it can be concluded that the Pd films deposited on SiO_2/Si and PI-SiO_2/Si substrates with a relatively rough surface have a more open columnar structure than Pd film on the smoother Ti-SiO_2/Si substrate. Here the small irregularities on the substrate act as extra nucleation sites enhancing the formation of an open columnar structure [60].

Crystallographic texture

Fig. 3 presents fiber texture plots (FTP) of the Pd-{111} reflection for both series-1&2 as-deposited films. The strength and sharpness of the (111) fiber texture is more pronounced for series-1 as compared to series-2 films. From the series-1 films, the Pd-SiO_2/Si and Pd-Ti-SiO_2/Si, show the strongest textured. FTP of all series-2 films indicates that (111) fiber texture is weak and broad. The fraction of randomly oriented grains is much larger for series-2 films than series-1, as presented in the inset Fig. 3. The deposition pressure is clearly the cause of the substantial difference in texture strength and sharpness. All in all, the low sputter pressure (series-1) leads to a closed columnar morphology with a strong and sharp fiber textured film, and the high sputter pressure (series-2) leads to a weak and broad fiber textured film with an open columnar morphology.

The sharpness of the texture is given in Table 1 by the half-width at half maximum, w, for the peak in the FTP at $\psi = 0°$. For Pd on PI layer, the (111) fiber texture is somewhat broader for both series-1&2 films as compared to those of Pd on SiO_2/Si and Pd on Ti-SiO_2/Si. This texture evolution could be assigned to the rougher surface of the PI-SiO_2/Si substrate. On a rough surface, shadowing effects and anisotropic diffusion of the adatoms lowers the degree of texture [61].

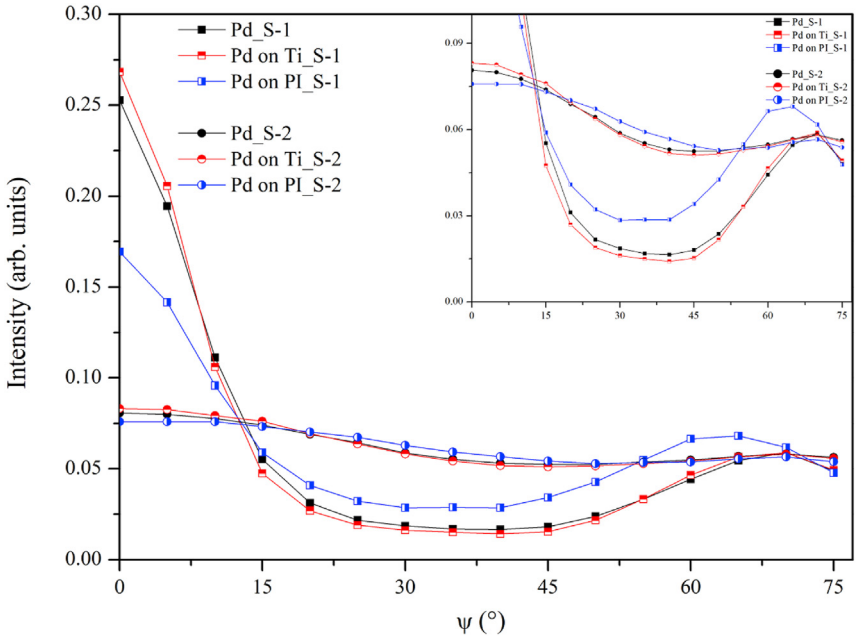

Fig. 3 – Pd-(111) fiber texture plot (FTP) of as-deposited series-1 and series-2 films deposited on SiO_2/Si, Ti-SiO_2/Si and PI-SiO_2/Si substrates. Series-1 (S-1) films show clearly peaks at $\psi = 0^\circ$ and $\psi = 70.5^\circ$ for (111) texture components. The inset shows series-2 (S-2) films with broad and weak fiber texture as compared to strong and sharp fiber texture for the series-1 films.

Stress

In Table 2, comparing the growth stress in the as-deposited series-1 and series-2 films, it was found that for series-1 (dense films), the in-plane stress ($\sigma_{//}$) is compressive, while for series-2 (open films) $\sigma_{//}$ is tensile.

For series-1, the values of the compressive growth stress are nearly the same for all Pd films (Table 2). This indicates that an intermediate layer has no major influence on growth stress when Pd is sputtered at low Ar pressure. In general, the intrinsic compressive stress observed in Zone T, dense film, is assigned to atomic peening during sputter deposition [62].

For series-2 films, the growth stress is tensile, and its magnitude depends on the type of intermediate layer (Table 2). Tensile stress observed in Zone 1, open (void-rich) film, is explained in terms of the grain boundary relaxation mechanism [38,62] and island coalescence [50]. The tensile stress is higher for Pd on Ti layer with a relatively less open columnar structure. However, when during deposition, more voided morphology forms, the tensile stresses generated are not sustained, and stress relaxation occurs. This is the case for Pd on PI layer and for Pd on a bare SiO_2/Si. The nature of the growth morphology and the magnitude of the stresses in the film are sensitive to the deposition conditions [62] and influence the mechanical strength of thin films [63].

Phase transformations: mechanical and thermal stability

When a Pd thin film is exposed to hydrogen, the α to β phase transition causes a volume increase of about 10 vol% [6]. Both the α-PdH_x phase and the β-PdH_x phase are of fcc structure [18]. The present study uses microscopic observations (TEM and SEM), measurements of the macro-stress, and the lattice defect densities to find out how hydrogen absorption and desorption of nanocrystalline Pd thin films might be influenced by their sputter deposition conditions and the underlying intermediate layer when deposited on a stiff substrate.

Room temperature

Visual observations of the Pd film topographic changes caused by hydrogen absorption were made through the transparent foil of the custom-made holder of *in-situ* XRD set-up (section Room temperature). Series-1 Pd film on bare SiO_2/Si substrate subjected to hydrogen loading at RT showed buckle formation. In Fig. 4(a–c) photographs made with 2 min interval displayed a gradual buckling (shiny silver areas) of the Pd film surface starting from edges and growing towards the center, Fig. 4(b). The entire film specimen was found buckle-delaminated after completion of the α→β phase transformation within 10 min, Fig. 4(c). After hydrogen deloading, some buckles flattened, but still, features of the buckled patterns are visible in Fig. 4(d). The *ex-situ* SEM analysis showed buckled and delaminated areas randomly scattered over the film surface in Fig. 4(j). In the compact series-1 films, the lack of voids to accommodate the expansion due to β-PdH_x phase formation during hydrogen uptake causes the building-up of compressive stress (Table 2). Only the Pd film on SiO_2/Si substrate β-phase showed buckling and delamination that causes the release of stress, see Table 2. The strong adhesion by the intermediate layers of Ti and PI prevents delamination (Fig. 4 (e-f)) and these films show a strong increase in the compressive stress (Table 2).

The more voided series-2 film on a bare SiO_2/Si substrate did not show any hydride-related topographical changes, and the surface remained flat during and after hydrogen is cycled,

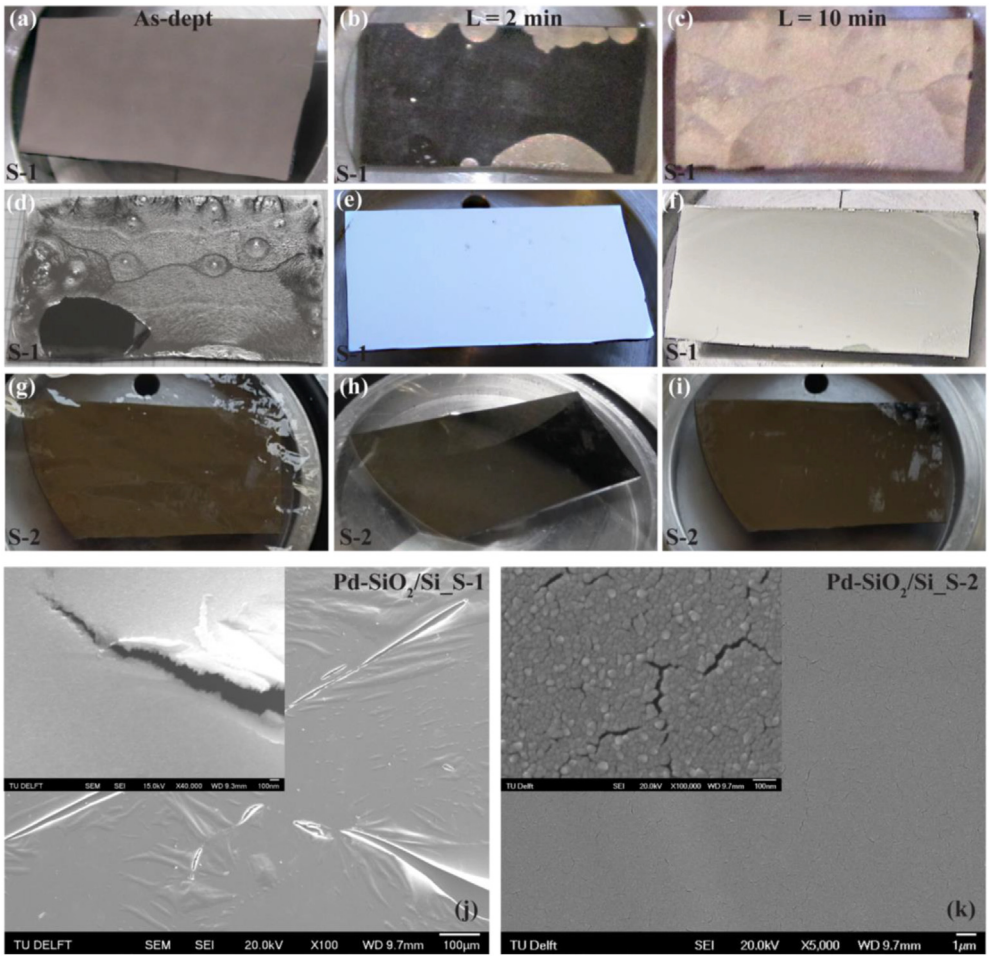

Fig. 4 – Room-temperature single cycle of hydrogen loading/deloading. For visualization of the topography changes, specimen pictures were made through the XRD radiation box: (a–f) Series-1 (S-1) films: Pd-SiO_2/Si (a) as-deposited, b) during H-loading within 2 min interval shows gradual blistering (color contrast) of the Pd layer from the substrate, (c) complete H-loading in 10 min shows blistered pattern throughout the film surface. (d–f) after H-L/D cycle: (d) Pd-SiO_2/Si still shows features of the blistered pattern, (e) Pd-Ti-SiO_2/Si and (f) Pd-PI-SiO_2/Si shows smooth surface as in the as-deposited state. (g–i) Series-2 (S-2) film Pd-SiO_2/Si: (g) in as-deposited condition, (h) during H-loading and (i) after H-L/D cycle. (j–k) *Ex-situ* SEM images of Pd-SiO_2/Si films after loading/deloading cycle: (j) series-1 (S-1) showing buckled and cracked surface in a large image (100 μm scale) and delaminated area in inset image (100 nm) and (k) series-2 (S-2) showing the flat surface in a large image (1 μm scale) and film morphology like in the as-deposited condition (Fig. 2(b)) in inset image (100 nm scale). (For interpretation of the references to color in this figure legend, the reader is referred to the Web version of this article.)

Fig. 4(g–i). In the supplemental information (Fig. S1) the diffraction patterns of series-1 and 2 for Pd on SiO_2/Si confirm the effect of buckling in the series-1 film and the integrity of the series-2 film. SEM image in Fig. 4(k) shows the flat surface topography of series-2 film. The presence of space in the form of tapered voids along grain boundaries (Fig. 1(c)) allows the relaxation of strains (Table 2).

The magnitude of structural deformation in compact films (series-1) was controlled by adding an adhesive intermediate layer between the film and the substrate. Fig. 5(a) shows a schematic representation of series-1 films deposited with and without an intermediate layer: SiO_2/Si, Ti-SiO_2/Si and PI-SiO_2/Si. Here and in earlier work [40], we found that for Pd on Ti layer, the α→β phase transformation was very slow and incomplete (a fraction of α-phase was not transformed). A similar observation was made in this work for Pd on PI layer; it took about 18 h to complete transformation into the β-phase. The slow hydride formation in these films is attributed to the compact morphology and the effect of clamping by the underlying adhesive intermediate layer that hinders lateral film expansion [26].

Table 1 – The half-width at half maximum (*w*) from Pd-(111) fiber texture plot in Fig. 3 at $\psi = 0^\circ$ for Pd films on SiO_2/Si substrate with and without intermediate layer deposited at 0.4 Pa Ar pressure (series-1) and 3 Pa Ar pressure (series-2).

As-deposited Pd films	SiO_2/Si	Ti-SiO_2/Si	PI-SiO_2/Si
Series-1, w	9.6	9.2	13.6
Series-2, w	22.7	22.3	28.4

Table 2 – In-plane stress, $\sigma_{//}$, for Pd films on SiO_2/Si substrate with and without intermediate layer during a single cycle of hydrogen loading/deloading at room-temperature. Pd film deposited at 0.4 Pa Ar pressure (series-1) and 3 Pa Ar pressure (series-2).

$\sigma_{//}$(MPa)	Series-1			Series-2		
	SiO_2/Si	Ti-SiO_2/Si	PI-SiO_2/Si	SiO_2/Si	Ti-SiO_2/Si	PI-SiO_2/Si
As-deposited	−21 ± 9	−17 ± 34	−18 ± 10	43 ± 13	117 ± 13	95 ± 18
Loading	23 ± 8	−462 ± 28	−471 ± 23	17 ± 18	−88 ± 16	−50 ± 14
Deloading	200 ± 8	563 ± 20	655 ± 14	61 ± 19	380 ± 3	305 ± 8

In series-2 films, the open columnar morphology is the dominating factor that surpasses the strong adhesion energy of the clamped film to the substrate, thus allowing free expansion of the film during loading and also channel stress release in Pd layer (Table 2). Series-2 films with an intermediate layer showed relatively fast α→β phase transformation, and it took about 15–20 min to complete the transformation. These films showed no traces of buckling or film detachment as have been reported in the literature [29,35,36]. The thermal stability of series-2 films is discussed in the next section.

Above room temperature

Phase transitions: 303 K–353 K (PT-only). The film morphology and intermediate layer have a profound effect both on the hydrogen uptake response and mode of deformation in the Pd thin film system at room temperature. Here phase transitions were studied up to the critical temperature [6,7] in series-2 films. Films were heated from 303 K to 353 K (in steps of 10 K) and subsequently cooled down to 303 K in the H_2/N_2 gas mixture. When the gas atmosphere was changed from N_2 gas to H_2/N_2 gas mixture at the starting temperature, 303 K, the diffraction patterns revealed an immediate α to β-phase transition. Upon step-wise heating, in H_2/N_2 gas, the critical temperature was reached, and the β to α-phase transition occurred at 333 K. While cooling down from 353 K, the α to β-phase transition occurred at a lower temperature 313 K. At 303 K, the gas atmosphere was changed to N_2 gas, and the β to α-phase transition occurred. Thus, in a PT-only experiment (303 K→ 353 K → 303 K), two cycles of hydrogen loading/deloading were covered, *i.e.*, α→β, β →α, α→β, β →α (Fig. 6(a)).

For all series-2 films, the material was fully transformed (from α to β and vice versa). The α→β phase transition in Pd films without intermediate layer and with PI intermediate layer was completed in about 12 min. Phase transformation was incomplete for Pd film strongly clamped on Ti-SiO_2/Si substrate and took about 30 min to reach the maximum amount of β-PdH_x hydride phase. This is in agreement with a previous observation that a Ti intermediate layer slows down the kinetics of hydrogen absorption/desorption significantly [40]. This slow kinetics is attributed both to the substrate clamping and Pd film morphology. For Pd on Ti layer with the dense bottom half (30–40 nm) and porous top half morphology [40], the formation of the β-PdH_x phase took approx. 120 min and a large fraction of α-PdH_x phase remained despite the fact that the film was kept for several hours in the H_2/N_2 gas atmosphere. This means open columnar structures largely contributes to improved response time and allows formable expansion during hydrogenation [6] when between α and β phases, a lattice mismatch of 3.5% generates large compressive stresses. These observations highlight that hydrogen uptake is strongly correlated to the film morphology.

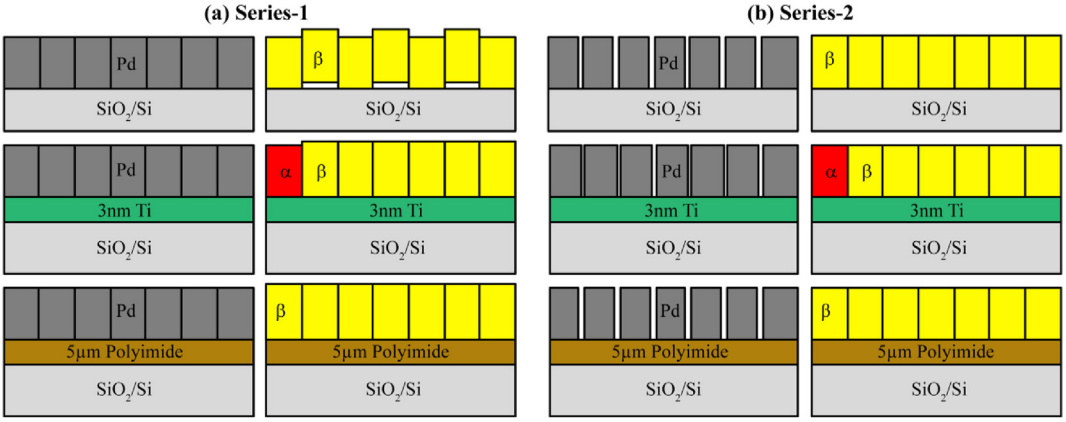

Fig. 5 – A pictorial description of our Pd films on SiO_2/Si, Ti-SiO_2/Si, and PI-SiO_2/Si substrates (top to bottom). (a) Series-1: left-side are as-deposited Pd films (grey: metallic, no H) with compact columnar morphology, and right-side are hydrogen-loaded Pd(H) films (yellow: high-H β-phase; red: low-H α-Phase) in the H_2/N_2 gas mixture for 10 min leading to buckling formation (Pd on bare SiO_2/Si), 420 min (Pd on Ti) and 1100 min (Pd on PI) respectively. Pd films with Ti and PI intermediate layer remained smooth as in the as-deposited state. (b) Series-2: left-side are as-deposited films with open columnar morphology and the right-side are hydrogen-loaded Pd films in the H_2/N_2 gas mixture. All series-2 films remained flat during loading without buckle formation. (For interpretation of the references to color in this figure legend, the reader is referred to the Web version of this article.)

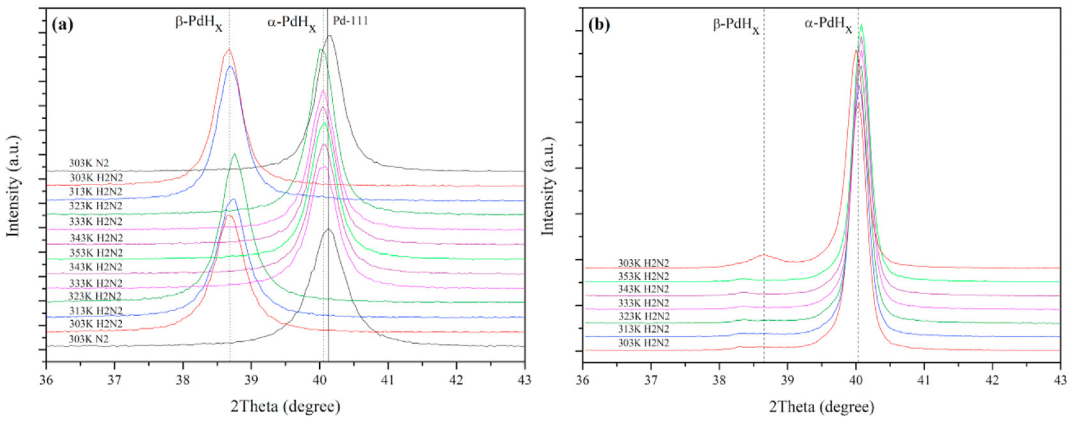

Fig. 6 – XRD scans showing the {111} reflections of the β-phase and the α-phase for series-2 films: (a) complete α↔β phase transitions are observed for Pd-SiO_2/Si and Pd-PI-SiO_2/Si films both for PT-only and HT+PT, and (b) for Pd-Ti-SiO_2/Si film α↔β phase transitions are suppressed after annealing film at 623 K for 18 h followed by PT (HT+PT).

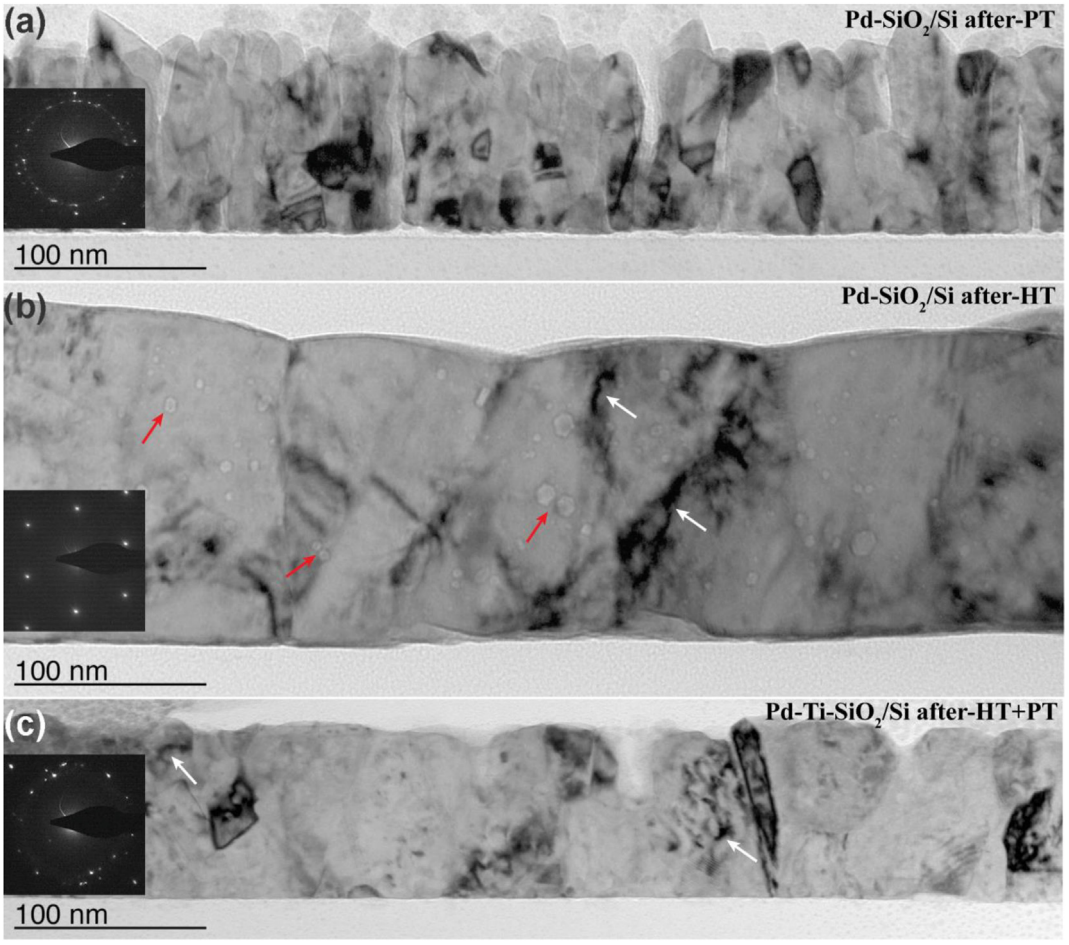

Fig. 7 – The cross-sectional view of TEM bright-field images of series-2 Pd films. Pd-only expt.: (a) Pd-SiO_2/Si film after phase transitions (after-PT): film morphology and grain size remains unchanged. HT+PT expt.: (b) Pd-SiO_2/Si film after annealing at 623 K for 18 h (after-HT): grain coalescence, loss of open columnar morphology and formation of spherical nanopores highlighted by red arrows, and (c) Pd-Ti-SiO_2/Si film after phase transitions on annealed (623 K for 18 h) film (after-HT+PT): formation of compact morphology like as-deposited series-1 film, in such morphology α↔β phase transitions, are suppressed. White arrows are pointing to dislocation segments. (For interpretation of the references to color in this figure legend, the reader is referred to the Web version of this article.)

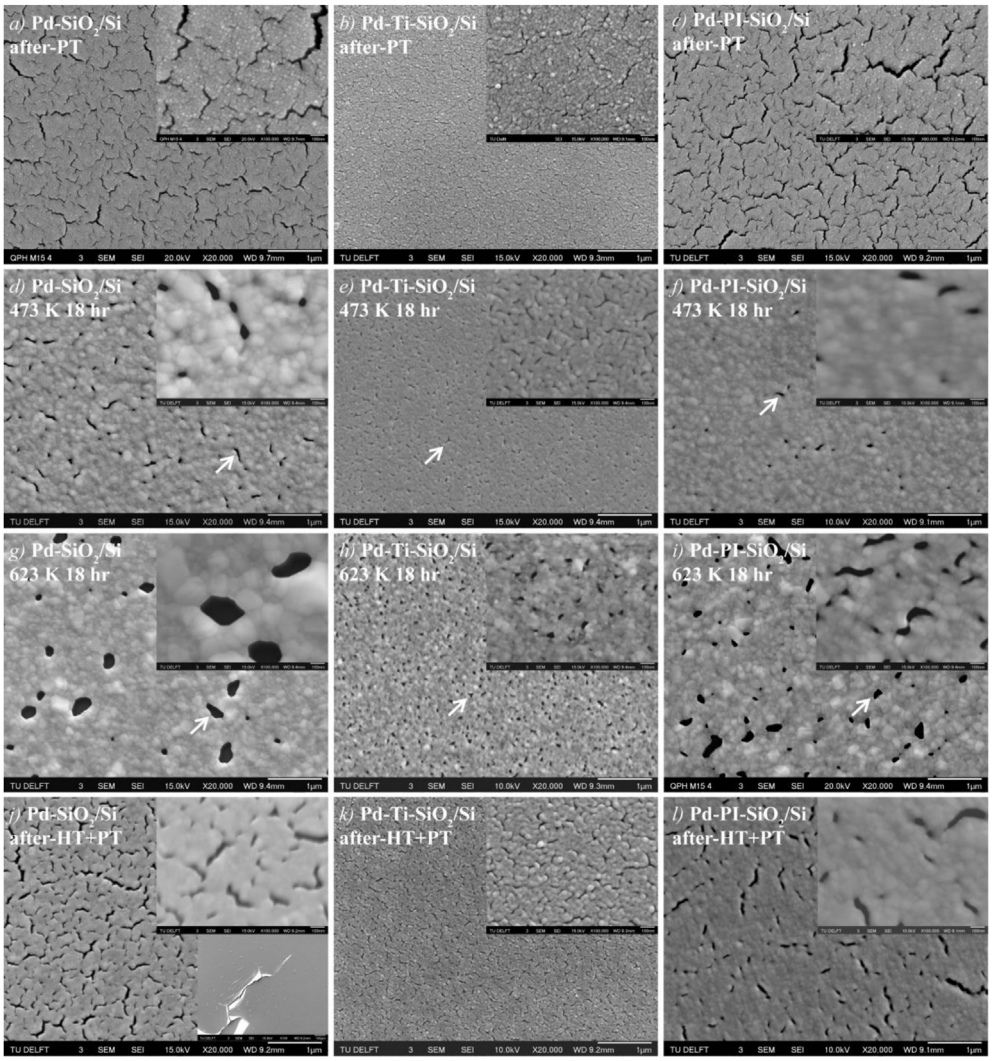

Fig. 8 – SEM surface morphologies of series-2 Pd films. The large images (1 μm scale) and the insets (100 nm scale) exemplify the morphological evolution in Pd films. From left to right: Pd-SiO_2/Si, Pd-Ti-SiO_2/Si and Pd-PI-SiO_2/Si films. From top to bottom: after phase transitions (after-PT), after annealing film at 473 K for 18 h, after annealing film at 623 K for 18 h, and after phase transitions on annealed (473 K for 18 h) film (after-HT+PT). The white arrows are showing annealing induced holes developed due to dewetting phenomena.

The TEM (Fig. 7(a)) and SEM (Fig. 8(a–c)) results showed that all Pd films remained morphologically unperturbed after the PT-only experiment, irrespective of the presence of an intermediate layer. For temperatures up to 353 K, neither coalescence nor growth of the grains occurred. We noticed, however, an increase in the primary microcrack spacing after-PT (Fig. 8(a&c) inset) as compared to as-deposited primary microcracks visible in Fig. 2(b&d). In particular, the crack density is higher for Pd-SiO_2/Si film than for Pd-PI-SiO_2/Si film, while no such crack formation was observed for Pd-Ti-SiO_2/Si film. The microcracks proliferate at pre-existing defects and propagate along grain or grain boundaries, indicating intergranular fracture [64]. The intergranular cracks are often interconnected, forming a network of microcrack that can be detrimental to the mechanical strength of the film. But stress relaxation by microcrack propagation in these films prevents subsequent crack networks from developing unless they are sufficiently far away for the strain energy to build to a critical level. In the case that no microcrack widening is observed for Pd with Ti intermediate layer (Fig. 8(b)), no stress release is observed (Table 3). The persistent increase of tensile stress most probably is also the cause of the slower hydrogen absorption in Pd on Ti layer.

Table 3 – Measured stresses in series-2 films in as-deposited condition, after phase transitions (after-PT) from PT-only experiment and after phase transitions on annealed films (after-HT+PT) from HT+PT experiment. Note that different specimens were used for PT-only and HT+PT experiment (taken from the same wafer).

Series-2 films	SiO_2/Si	Ti-SiO_2/Si	PI-SiO_2/Si
as-deposited, $\sigma_{//}$(MPa)	147 ± 5	210 ± 5	82 ± 7
after-PT, $\sigma_{//}$(MPa)	332 ± 5	451 ± 17	344 ± 20
after-HT+PT, $\sigma_{//}$(MPa)	5 ± 5	430 ± 13	408 ± 21

It is expected that on mechanically soft PI-SiO_2/Si substrate, crack propagation [65] is more likely than on a mechanically hard Ti-SiO_2/Si substrate. For Pd on PI layer, the large compliance of the polyimide layer can increase microcrack spacing rearrangements and distance over which stresses are relaxed in the neighborhood of a crack [66]. The ease of propagation of a crack channeling in a film also depends on underlying substrate mechanical properties besides the stresses generated.

High-temperature annealing prior to phase transitions (HT+PT). Thermal treatment at 473 K and 623 K reduced the number of as-deposited intercolumnar voids and more closed structures developed. In the annealed films, globular pores of various shapes and sizes unevenly scattered within the compact columnar structures are formed, Fig. 7(b). These pores are remnants of the voids present in the as-deposited film that coalesce as a result of annealing-induced grain growth. From SEM analysis, it was found that the initial grain boundary voids started disappearing within 2 h of annealing at 473 K.

From the cross-sectional view of TEM image in Fig. 7(b), one can see that annealing at 623 K led to significant grain growth (50–200 nm wide), closing the voids in the Pd film on a bare SiO_2/Si. The red arrows in the figure point to spherical nanopores sized in the range 1–15 nm. In contrast, no such spherical nanopores can be observed within the compact morphology of Fig. 7(c) for Pd-Ti-SiO_2/Si film after-HT+PT, and the average lateral grain size measured from BF-TEM images is in the range 25–65 nm. In Fig. 8(d–i), SEM images show that dewetting or agglomeration starts at 473 K. Small holes are indicated by the white arrows in Fig. 8(d–f), that develops further at 623 K temperature as shown in Fig. 8(g–i). Pd on Ti layer showed the smallest holes size with quite a uniform size distribution. The differences in the number and shapes of the holes reflect the differences in film-substrate interaction [67]. In particular, the strong adhesion of the film to the Ti intermediate layer limits dewetting.

The evolved morphology of the Pd thin film after annealing strongly influenced phase transitions and the film stability during hydrogen uptake in addition to the effect of the intermediate layer. HT+PT experiments were conducted by annealing Pd films at 473 K or 632 K followed by subsequent phase transitions (PT). For Pd on a bare SiO_2/Si after annealing, phase transitions remained unaffected, but Pd layer was found buckle-delaminated at the end of HT+PT (lower right corner inset image Fig. 8(j)). This behavior is similar to what was observed for series-1 Pd on a bare SiO_2/Si (Fig. 4(j)) with compact morphology after a single hydrogen loading/deloading cycle at RT (section Room temperature).

For Pd on Ti layer when annealed at 632 K, the XRD patterns in Fig. 6(b) show that phase transition is completely suppressed, as seen in Fig. 7(c), the film shows a compact morphology. In contrast, only partial suppression of phase transition occurred when annealed at 423 K. Similar observations were made earlier by Kim et al. [35] for Pd films with Ti intermediate layer, but the suppression of phase transition then occurred in as-deposited film at RT. At the same time, Pd on PI layer after annealing at 473 K exhibits complete phase transitions without buckle-induced delamination.

For Pd-SiO_2/Si and Pd-PI-SiO_2/Si films after-HT+PT (Fig. 8(j&l)), the tapered voids and microcracks that during annealing disappeared and formed large globular pores, reappeared as wide microcracks. These cracks indicate an effective mechanism for stress reduction locally. However, due to poor adhesion of Pd film on a SiO_2/Si substrate, a crack + buckle network propagates, leading to eventual film delamination. For Pd on PI layer (Fig. 8(l)), however, no buckling occurs. Since we did not observe delamination after phase transitions even for compact morphology, we argue that the presence of the intermediate polymer layer helps in delocalizing the hydrogen-induced strain in the Pd film. Hence, a Pd film with a flexible PI intermediate layer exhibits free-standing film-like behavior besides being strongly clamped on a stiff SiO_2/Si substrate.

Microstructure from XRD line-broadening

The microstructural investigation was performed for the series-2 films only because the delamination occurring in series-1 films prevents practical application. Modified Williamson-Hall (Mod-WH) plots for the PT-only and HT+PT experiments were prepared by analyzing the line widths and applying formula (3) (see section X-ray diffraction (XRD)) for all possible types of dislocations. On the basis of weighted least-square fitted straight lines using the estimated standard deviations in the breadth, it was concluded that randomly oriented pure screw dislocations of the {111}, a/2<110> slip system led to the best fits for all series-2 films studied.

The mod-WH plots in (Fig. 9) show the analogies and differences in the microstructural behavior of the three film systems. In Fig. 10(a) (and supplementary Table S2), the values of crystallite size $\langle D \rangle$ and dislocation density ρ obtained from Fig. 9 by a weighted least-square fitting of straight lines are shown. To visualize changes, in Fig. 10(b), the $\langle D \rangle$ and ρ values are given relative to the average $\langle D \rangle$ and ρ values of the as-deposited state of the PT and HT+PT samples (taken from the same wafer).

The as-deposited films (as-dept.) of Pd-Ti-SiO_2/Si and Pd-PI-SiO_2/Si exhibit almost identical $\langle D \rangle$ and ρ, whereas for Pd-SiO_2/Si, the $\langle D \rangle$ is smaller and ρ is larger (Fig. 10(a)). This implies that the intermediate layers reduce the formation of dislocations during deposition. This agrees with the idea that without clamping by an intermediate layer, free space around the columns can be used to generate dislocations and allow some crystallite growth (reduction of (e.g., mosaic) boundaries). And this agrees with the differences of the stresses (see Table 3). After PT (PT-only), an overall decrease of the slope is observed in Fig. 9, for Pd-SiO_2/Si and Pd-PI-SiO_2/Si, implying a decrease in dislocation densities, whereas the slope increases for Pd-Ti-SiO_2/Si. This agrees with the idea that the clamping is more rigid for Ti so that the phase transition to the β-phase is accommodated by dislocations. For all series-2 films $\langle D \rangle$ hardly changes (Fig. 10(a and b)).

The trends observed in the mod-WH for the HT+PT experiments are similar for all specimens. The heat treatment reduces the slope and intercept, and the subsequent PT results in an increase in the slope. The high-temperature annealing (after-HT) induced grain growth leads to a considerable increase in $\langle D \rangle$, and reduction of dislocation densities.

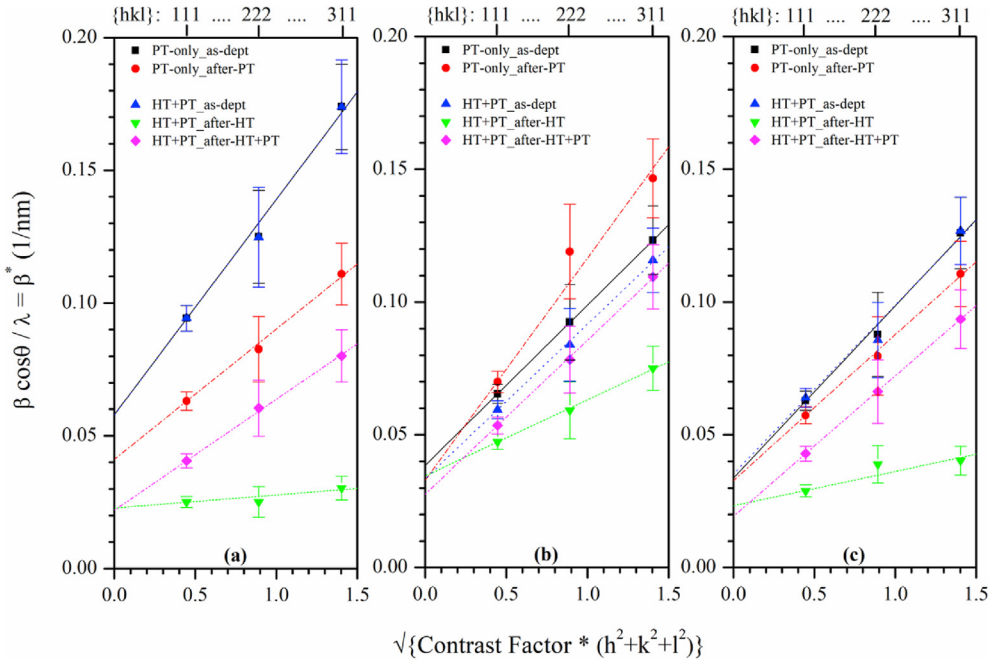

Fig. 9 – The mod-WH plots for the series-2 films: (a) Pd-SiO_2/Si, (b) Pd-Ti-SiO_2/Si and (c) Pd-PI-SiO_2/Si showing β^*_{hkl}, versus C_{hkl} for randomly oriented screw dislocations with Burgers vector a/2<110> and glide plane {111}. Note that different specimens were used for PT-only and HT+PT experiments. The error bars shown are +3 and −3 times the standard deviation (see Eq. (3)).

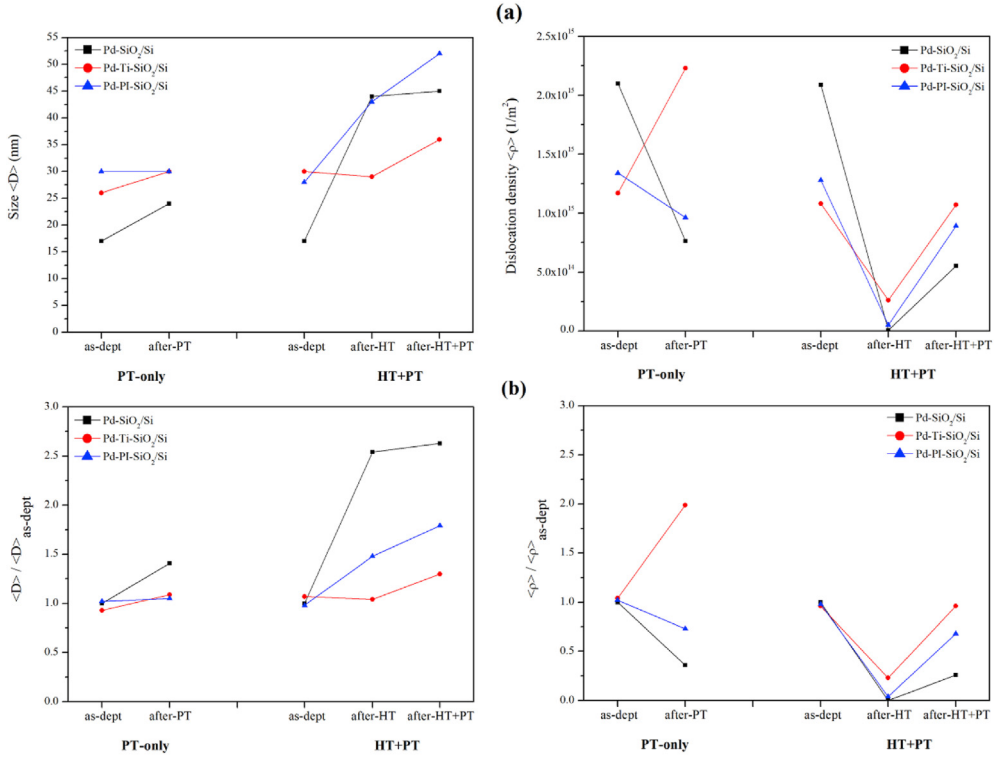

Fig. 10 – (a) Plots with the absolute values of the crystallite size < *D* > (left) and the dislocation density ρ (right) for each of the three Pd film systems during PT-only and HT+PT experiments. Error bars that follow from the error bar shown in Fig. 9 are not shown, but are 20–50% of the values shown and can be found in supplementary Table S2. (b) Plots with the < *D* > (left) and ρ (right) values relative to the average value obtained from the combination of as-deposited specimens used in PT-only and HT+PT experiments for each Pd film system.

The subsequent PT slightly increase the <*D*>. The deformation due to the phase transition causes the dislocation density to increase (Fig. 10(b)).

Comparing the overall effects of both experiments, the <*D*> and ρ values for Pd-PI-SiO_2/Si are always between the results for Pd film without an intermediate layer and with a Ti intermediate layer (Fig. 10(b)).

Deformation mechanism

Whereas much of the mechanical behavior (i.e., buckling, delamination, and macro-stresses in section Above Room temperature) of the three Pd film systems are explained on a μm scale as related to the TEM and SEM observations of series-2 (Fig. 1(c–e) & Figs. 7 and 2(b–d) & Fig. 8), the above section endorses microstructural interpretation (<*D*> and ρ) on a nm scale. The modified-WH plots indicate that in Pd films, microstrain is caused by the presence of dislocations. Colla et al. [68], using time-resolved HRTEM, demonstrated that the dislocation-mediated mechanism dictates the mechanical stability both during hydrogen loading (deformation) and deloading (relaxation) in textured Pd thin films.

Deformation during phase transitions (PT-only)
The dislocation densities obtained show a decrease after-PT for the Pd film on a bare SiO_2/Si and for Pd on PI layer as compared to the as-deposited state, whereas a Pd on Ti layer shows an increase in dislocation density, Fig. 10(b). This shows that the decrease in microstrain (dislocation density) for Pd-SiO_2/Si could be caused by the added free surface generated by microcracks (see Fig. 8(a)) propagating through voided grain boundaries.

The Pd on PI layer shows a small decrease in dislocation density after-PT (Fig. 10(b)). Almost no microcracks were observed (Fig. 8(c)), suggesting that the initial as-deposited defects would be confined at the interface of grain boundaries, hindering, relaxation and cracking, which suggests that a PI layer allows some of the strain relaxation inside the Pd crystallites by its flexibility. For Pd on Ti layer, an increase in strain and dislocation density after-PT is found (Table 3, Fig. 9(b)). The loose columnar morphology of Pd film allowed phase transitions even on a rigid Ti-SiO_2/Si substrate. Due to strong film to substrate bonding, cracks are not generated to relax hydrogen-induced stresses. The dislocations generated during loading (deformation) are blocked by the rigid substrate and dislocations pile-up against the film-substrate interface.

Thus, it appears possible that the increase of the bonding to the substrate by an intermediate layer of Ti or PI in our series-2 thin film systems, a microstructural stabilization mechanism occurs that implies some freedom to expand/contract during hydrogen loading/deloading so that some stress relaxation occurs along open grain boundaries. In this way, Pd films with an open morphology successfully restrict stresses from amplifying, and no noticeable structural deformation occurred.

Deformation in annealed Pd thin films (HT+PT)
Besides microstructural strengthening, the interaction at the film-substrate interface is also critical in attaining a stable metal thin film system [30]. For all series-2 films after annealing, the XRD profiles exhibit a reduction in line breadth (Fig. 9); this change is associated with an increase in crystallite size and dislocation density decrease (Fig. 10). This reduction is particularly substantial for Pd films on a bare SiO_2/Si and, to some extent, also for Pd on PI layer. In both cases, it is a reasonable assumption that the loss of defects occurs rapidly because of the added free surfaces along disconnected microcracks or nanopores, as seen in Fig. 8(d and f) formed by grain agglomeration [69]. However, the lattice strain (Table 3) remained relatively high for Pd on Ti layer. In this case, the film-substrate interface plays a key role in the dislocation evolution. According to Freund [70] and Nix [71], the motion of threading dislocations is confined in the metallic film by a stiff substrate. A hard and strongly adhering Ti-SiO_2/Si substrate provided higher repulsion for dislocations at the interface than for film attached on a soft and flexible surface (PI) or a substrate with poor adherence (SiO_2/Si).

The densities of pre-existing dislocations that decreased during annealing were strongly increased upon subsequent phase transitions (after-HT+PT) for all series-2 films. The pre-annealed Pd film on a bare SiO_2/Si, release stress and defects by local film detachment due to low adhesion. Thus, here the increase in dislocation density cannot be explained as stated earlier by the dislocation escape theory at the buckle-delaminated free surface. The increase in dislocation density can be explained in terms of dislocation nucleation at the grain boundaries. For annealed Pd on Ti layer, partial suppression of phase transitions causes limited dislocation activity, resulting in the slight increase of the lattice strain reaching the initial value as observed in the as-deposited film (Fig. 10(b)). In loaded Pd on PI layer, movement of dislocations at the Pd-film and PI-layer interface is the dominating stress relaxation pathway. Here, the interface plays a dominating role as the polyimide layer does not provide an obstacle for dislocations to escape the Pd film. The PI layer allowed Pd films to "breathe" during hydrogen absorption and desorption along with providing sufficient adhesion to the substrate. Here, the softer interface corresponds to the stronger thin film system.

Conclusion

In-situ X-ray diffraction study combined with SEM and TEM analysis on Pd thin films exposed to hydrogen showed that the interplay between film-microstructure and film-substrate interaction has a profound effect both on the response of hydrogen uptake and mode of damage. Stabilization against buckle-formation in compact morphology Pd film was achieved by adding an adhesive intermediate layer. It leads, however, to slow down (in the case of an intermediate layer) or partial suppression (in the case of a rigid layer) of phase transitions. The absence of buckle-delamination during Pd lattice expansion suggested that compressive stress-induced structural deformations are inhibited due to open columnar morphology of Pd film on a stiff SiO_2/Si substrate. But such Pd film under the influence of concurrent buckling and cracking delaminates above critical stress during high-temperature (623 K) H-loading due to weak adhesion. Inserting a flexible

adhesive polyimide layer, maintained adhesion, and absorption/desorption properties at elevated temperatures.

X-ray line-broadening analysis, used for defect studies, indicated that all Pd films contain similar kinds of defects (dislocations) but differ by defect density. The differences are mainly caused by differences in adherence to the substrate. A strongly adhering Ti-SiO_2/Si substrate provided higher repulsion for dislocations at the interface than for film attached on a flexible substrate (PI-SiO_2/Si) or on to a substrate with poor adherence (SiO_2/Si). Furthermore, the lowest concentration of the defects was found in the Pd-PI-SiO_2/Si film because the polymer substrate does not provide a strong obstacle for dislocations to escape the Pd film at the film-substrate interface. The Pd-PI interface acted as a perfect free surface for Pd film. Thus, a good combination of film microstructure and choice of intermediate layer allows upgrading Pd thin film systems mechanical strength.

Declaration of competing interest

The authors declare that they have no known competing financial interests or personal relationships that could have appeared to influence the work reported in this paper.

Acknowledgments

We would like to acknowledge the technical assistance provided by R.W.A. Hendrikx and R.M. Huizenga during the X-ray diffraction measurements. This work is financially supported by the Delft University of Technology.

Appendix A. Supplementary data

Supplementary data to this article can be found online at https://doi.org/10.1016/j.ijhydene.2020.10.163.

APPENDIX

Calculation of C_{hkl} values

Tables of C_{hkl} have been published for several types of Burgers vectors and glide planes for untextured cubic materials that contain randomly distributed dislocations (see Tables 2 and 4 of [54] and Tables I and II, III, and IV of [72]). However, some of these tables contain several rather obvious mistakes and therefore, we recalculated the erroneous values using the program Anizc [73] for all types of dislocations, with the exception of randomly oriented screw dislocations with a <110> Burgers vector. For these dislocations, we used the simple formulas for the C_{hkl} values for published by Scardi et al. [74]:

$$C_{h00} = \sqrt{A_i} / 6 \quad (A.1)$$

$$q = 3{-}2 / A_i \quad (A.2)$$

where A_i is the Zener ratio, characteristic of elastic anisotropy (A_z in Ref. [54,72]).

The calculations of all other *HKL_contrast_factors* C_{hkl} is based on the formula (just as in Ref. [54,72]):

$$C_{hkl} = C_{h00} - C_{h00}.q.H \quad (A.3)$$

where $H = (h^2k^2 + h^2l^2 + k^2l^2)/(h^2+k^2+l^2)^2$ and q is a constant.

The parametrization of C_{h00} and q proposed by Ungar et al. [54] is superfluous when determining the "average contrast factors" for dislocation with a random orientation distribution in an untextured cubic material. Then it is simpler and quicker to use only the appropriate C_{111} and C_{h00}, because:

1) two small tables are required for each slip system to obtain sufficiently accurate values for C_{h00} and C_{111}; i.c., one table for C_{h00}, for all practically possible values of A_z (see text below *eq* (A2); 13 values between 0 and 10) and c_{12}/c_{44} (4 values between 0 and 5) and the analogous table for C_{111} [*see:* Supplementary Table S1].
2) *and q can be calculated simply from:*

$$q = \{(C_{111} / C_{h00}) - 1\} / 0.33333 \quad (A.4)$$

REFERENCES

[1] Ball M, Weeda M. The hydrogen economy—vision or reality? Int J Hydrogen Energy 2015;40:7903–19. https://doi.org/10.1016/j.ijhydene.2015.04.032.
[2] Adams BD, Chen A. The role of palladium in a hydrogen economy. Mater Today 2011;14:282–9. https://doi.org/10.1016/S1369-7021(11)70143-2.
[3] Abe J, Popoola A, Ajenifuja E, Popoola O. Hydrogen energy, economy and storage: review and recommendation. Int J Hydrogen Energy 2019;44:15072–86. https://doi.org/10.1016/S1369-7021(11)70143-2.
[4] Lischka M, Groß A. Hydrogen on palladium: a model system for the interaction of atoms and molecules with metal surfaces. Recent developments in vacuum science and Technology. Research Signpost; 2003. p. 111–32.
[5] Jewell LL, Davis BH. Review of absorption and adsorption in the hydrogen–palladium system. Appl Catal Gen 2006;310:1–15. https://doi.org/10.1016/j.apcata.2006.05.012.
[6] Manchester F, San-Martin A, Pitre J. The H-Pd (hydrogen-palladium) system. J Phase Equil 1994;15:62–83. https://doi.org/10.1007/BF02667685.
[7] Flanagan TB, Oates W. The palladium-hydrogen system. Annu Rev Mater Sci 1991;21:269–304. https://doi.org/10.1146/annurev.ms.21.080191.001413.
[8] Zhao M, Sloof WG, Böttger AJ. Modelling of surface segregation for palladium alloys in vacuum and gas environments. Int J Hydrogen Energy 2018;43:2212–23. https://doi.org/10.1016/j.ijhydene.2017.12.039.
[9] Burkhanov GS, Gorina NB, Kolchugina NB, Roshan NR, Slovetsky DI, Chistov EM. Palladium-based alloy membranes for separation of high purity hydrogen from hydrogen-containing gas mixtures. Platin Met Rev 2011;55:3–12. https://doi.org/10.1595/147106711X540346.

[10] Baldi A, Dam B. Thin film metal hydrides for hydrogen storage applications. J Mater Chem 2011;21:4021–6. https://doi.org/10.1039/C0JM03249B.
[11] Jang B, Cho S, Park C, Lee H, Song M-J, Lee W. Palladium nanogap-based H2 sensors on a patterned elastomeric substrate using nanoimprint lithography. Sensor Actuator B Chem 2015;221:593–8. https://doi.org/10.1016/j.snb.2015.06.142.
[12] Edwards PP, Kuznetsov VL, David WI, Brandon NP. Hydrogen and fuel cells: towards a sustainable energy future. Energy Pol 2008;36:4356–62. https://doi.org/10.1016/j.enpol.2008.09.036.
[13] Okazaki J, Ikeda T, Tanaka DAP, Sato K, Suzuki TM, Mizukami F. An investigation of thermal stability of thin palladium–silver alloy membranes for high temperature hydrogen separation. J Membr Sci 2011;366:212–9. https://doi.org/10.1016/j.memsci.2010.10.011.
[14] Al-Mufachi N, Rees N, Steinberger-Wilkens R. Hydrogen selective membranes: a review of palladium-based dense metal membranes. Renew Sustain Energy Rev 2015;47:540–51. https://doi.org/10.1016/j.rser.2015.03.026.
[15] Rusman N, Dahari M. A review on the current progress of metal hydrides material for solid-state hydrogen storage applications. Int J Hydrogen Energy 2016;41:12108–26. https://doi.org/10.1016/j.ijhydene.2016.05.244.
[16] Rahimpour M, Samimi F, Babapoor A, Tohidian T, Mohebi S. Palladium membranes applications in reaction systems for hydrogen separation and purification: a review. Chem Eng Process: Process Intensification 2017;121:24–49. https://doi.org/10.1016/j.cep.2017.07.021.
[17] Fernandez E, Helmi A, Medrano J, Coenen K, Arratibel A, Melendez J, et al. Palladium based membranes and membrane reactors for hydrogen production and purification: an overview of research activities at Tecnalia and TU/e. Int J Hydrogen Energy 2017;42:13763–76. https://doi.org/10.1016/j.ijhydene.2017.03.067.
[18] Pundt A, Kirchheim R. Hydrogen in metals: microstructural aspects. Annu Rev Mater Res 2006;36:555–608. https://doi.org/10.1146/annurev.matsci.36.090804.094451.
[19] Kirchheim R, Mütschele T, Kieninger W, Gleiter H, Birringer R, Koble T. Hydrogen in amorphous and nanocrystalline metals. Mater Sci Eng 1988;99:457–62. https://doi.org/10.1016/0025-5416(88)90377-1.
[20] Iwaoka H, Arita M, Horita Z. Hydrogen diffusion in ultrafine-grained palladium: roles of dislocations and grain boundaries. Acta Mater 2016;107:168–77. https://doi.org/10.1016/j.actamat.2016.01.069.
[21] Ulvestad A, Yau A. The self-healing of defects induced by the hydriding phase transformation in palladium nanoparticles. Nat Commun 2017;8:1–6. https://doi.org/10.1038/s41467-017-01548-7.
[22] Narayan TC, Hayee F, Baldi A, Koh AL, Sinclair R, Dionne JA. Direct visualization of hydrogen absorption dynamics in individual palladium nanoparticles. Nat Commun 2017;8:14020. https://doi.org/10.1038/ncomms14020.
[23] Amin-Ahmadi B, Connétable D, Fivel M, Tanguy D, Delmelle R, Turner S, et al. Dislocation/hydrogen interaction mechanisms in hydrided nanocrystalline palladium films. Acta Mater 2016;111:253–61. https://doi.org/10.1016/j.actamat.2016.03.054.
[24] Hamm M, Burlaka V, Wagner S, Pundt A. Achieving reversibility of ultra-high mechanical stress by hydrogen loading of thin films. Appl Phys Lett 2015;106:243108. https://doi.org/10.1063/1.4922285.
[25] Pedersen TL, Liesch C, Salinga C, Eleftheriadis T, Weis H, Wuttig M. Hydrogen-induced changes of mechanical stress and optical transmission in thin Pd films. Thin Solid Films 2004;458:299–303. https://doi.org/10.1016/j.tsf.2003.12.040.
[26] Wagner S, Pundt A. Quasi-thermodynamic model on hydride formation in palladium–hydrogen thin films: impact of elastic and microstructural constraints. Int J Hydrogen Energy 2016;41:2727–38. https://doi.org/10.1016/j.ijhydene.2015.11.063.
[27] Wagner S, Kramer T, Uchida H, Dobron P, Cizek J, Pundt A. Mechanical stress and stress release channels in 10–350 nm palladium hydrogen thin films with different microstructures. Acta Mater 2016;114:116–25. https://doi.org/10.1016/j.actamat.2016.05.023.
[28] Pivak Y, Schreuders H, Slaman M, Griessen R, Dam B. Thermodynamics, stress release and hysteresis behavior in highly adhesive Pd–H films. Int J Hydrogen Energy 2011;36:4056–67. https://doi.org/10.1016/j.ijhydene.2010.12.063.
[29] Pundt A, Nikitin E, Pekarski P, Kirchheim R. Adhesion energy between metal films and polymers obtained by studying buckling induced by hydrogen. Acta Mater 2004;52:1579–87. https://doi.org/10.1016/j.actamat.2003.12.003.
[30] Wong M-f, Duan G, Wan K-t. Adhesion–delamination mechanics of a prestressed circular film adhered onto a rigid substrate. J Adhes 2007;83:67–83. https://doi.org/10.1080/00218460601102878.
[31] Gremaud R, Gonzalez-Silveira M, Pivak Y, De Man S, Slaman M, Schreuders H, et al. Hydrogenography of PdHx thin films: influence of H-induced stress relaxation processes. Acta Mater 2009;57:1209–19. https://doi.org/10.1016/j.actamat.2008.11.016.
[32] Harumoto T, Shi J, Nakamura Y. Effects of stress and defects on hydrogenation and magnetic properties in (111) fiber-textured palladium cobalt alloy films. Int J Hydrogen Energy 2020;45:11662–74. https://doi.org/10.1016/j.ijhydene.2020.02.118.
[33] Čížek J, Melikhova O, Vlček M, Lukáč F, Vlach M, Procházka I, et al. Hydrogen-induced microstructural changes of Pd films. Int J Hydrogen Energy 2013;38:12115–25. https://doi.org/10.1016/j.ijhydene.2013.03.096.
[34] Delmelle R, Amin-Ahmadi B, Sinnaeve M, Idrissi H, Pardoen T, Schryvers D, et al. Effect of structural defects on the hydriding kinetics of nanocrystalline Pd thin films. Int J Hydrogen Energy 2015;40:7335–47. https://doi.org/10.1016/j.ijhydene.2015.04.017.
[35] Kim KR, Noh J-S, Lee JM, Kim YJ, Lee W. Suppression of phase transitions in Pd thin films by insertion of a Ti buffer layer. J Mater Sci 2010;46:1597–601. https://doi.org/10.1007/s10853-010-4970-x.
[36] Matsumoto I, Sakaki K, Nakamura Y, Akiba E. In situ atomic force microscopy observation of hydrogen absorption/desorption by Palladium thin film. Appl Surf Sci 2011;258:1456–9. https://doi.org/10.1016/j.apsusc.2011.09.103.
[37] Vlček M, Lukáč F, Vlach M, Wagner S, Uchida H, Baehtz C, et al. Influence of microstructure and mechanical stress on behavior of hydrogen in 500nm Pd films. J Alloys Compd 2015;645. https://doi.org/10.1016/j.jallcom.2014.12.086. S446-S9.
[38] Windischmann H. Intrinsic stress in sputter-deposited thin films. Crit Rev Solid State Mater Sci 1992;17:547–96. https://doi.org/10.1080/10408439208244586.
[39] Verma N, Böttger AJ. Stress development and adhesion in hydrogenated nano-columnar Pd and Pd/Ti ultra-thin films. Adv Mater Res 2014:996. https://doi.org/10.4028/www.scientific.net/AMR.996.872.
[40] Verma N, Krishnamurthy G, Tichelaar FD, Böttger AJ. Controlling morphology and texture of sputter-deposited Pd films by tuning the surface topography of the (Ti) adhesive layer. Surf Coating Technol 2019;359:24–34. https://doi.org/10.1016/j.surfcoat.2018.12.053.

[41] Delhez R, De Keijser TH, Mittemeijer E. Determination of crystallite size and lattice distortions through X-ray diffraction line profile analysis. Fresenius' Z für Anal Chem 1982;312:1–16. https://doi.org/10.1007/BF00482725.
[42] Scardi P, Leoni M, Delhez R. Line broadening analysis using integral breadth methods: a critical review. J Appl Crystallogr 2004;37:381–90. https://doi.org/10.1107/S0021889804004583.
[43] Diffrac.Eva. Bruker AXS software, karlsruhe, Germany. 2001. https://www.bruker.com/.
[44] Welzel U, Leoni M. Use of polycapillary X-ray lenses in the X-ray diffraction measurement of texture. J Appl Crystallogr 2002;35:196–206. https://doi.org/10.1107/S0021889802000481.
[45] PANalytical X'Pert Stress Plus. PANalytical, almelo, The Netherlands. 2012. https://www.malvernpanalytical.com/.
[46] Hauk V. Structural and residual stress analysis by nondestructive methods: evaluation-Application-Assessment. Elsevier; 1997. https://doi.org/10.1016/B978-0-444-82476-9.X5000-2.
[47] Hsu D, Leisure R. Elastic constants of palladium and β-phase palladium hydride between 4 and 300 K. Phys Rev B 1979;20:1339–44. https://doi.org/10.1103/PhysRevB.20.1339.
[48] Welzel U, Mittemeijer EJ. Diffraction stress analysis of macroscopically elastically anisotropic specimens: on the concepts of diffraction elastic constants and stress factors. J Appl Phys 2003;93:9001–11. https://doi.org/10.1063/1.1569662.
[49] Welzel U, Mittemeijer EJ. Applicability of the crystallite group method to fibre textured specimens. Materials science forum. Trans Tech Publ; 2004. p. 131–6. https://doi.org/10.4028/www.scientific.net/MSF.443-444.131.
[50] Igor Pro, WaveMetrics. Lake oswego, Oregon, USA. 2011. https://www.wavemetrics.com/.
[51] Srm660a. Lanthanum hexaboride powder line position and line shape standard for powder diffraction. Certificate. Gaithersburg, MD, USA: National Institute of Standards and Technology, US Department of Commerce; 2000. https://www.nist.gov/srm.
[52] Velterop L, Delhez R, Keijser THd, Mittemeijer E, Reefman D. X-ray diffraction analysis of stacking and twin faults in fcc metals: a revision and allowance for texture and non-uniform fault probabilities. J Appl Crystallogr 2000;33:296–306. https://doi.org/10.1107/S0021889800000133.
[53] Williamson G, Hall W. X-ray line broadening from filed aluminium and wolfram. Acta Metall 1953;1:22–31. https://doi.org/10.1016/0001-6160(53)90006-6.
[54] Ungár T, Dragomir I, Révész Á, Borbély A. The contrast factors of dislocations in cubic crystals: the dislocation model of strain anisotropy in practice. J Appl Crystallogr 1999;32:992–1002. https://doi.org/10.1107/S0021889899009334.
[55] Gubicza J. X-ray line profile analysis in materials science. Hershey, Pennsylvania: Engineering Science Reference; 2014. http://doi:10.4018/978-1-4666-5852-3.
[56] Petrov I, Barna P, Hultman L, Greene J. Microstructural evolution during film growth. J Vac Sci Technol 2003;21:S117–28. https://doi.org/10.1116/1.1601610.
[57] Thornton JA. Influence of apparatus geometry and deposition conditions on the structure and topography of thick sputtered coatings. J Vac Sci Technol 1974;11:666–70. https://doi.org/10.1116/1.1312732.
[58] Jones T, Hall K. The melting point of palladium and its dependence on oxygen. Metrologia 1979;15:161. https://doi.org/10.1088/0026-1394/15/3/007.
[59] Smith DL. Thin film deposition: principles and practice. McGraw-Hill Inc; 1995. https://doi.org/10.1063/1.2807590.
[60] Bai P, McDonald JF, Lu TM, Costa MJ. Effect of substrate surface roughness on the columnar growth of Cu films. J Vac Sci Technol, A 1991;9:2113–7. https://doi.org/10.1116/1.577235.
[61] Whitacre J, Rek Z, Bilello J, Yalisove S. Surface roughness and in-plane texturing in sputtered thin films. J Appl Phys 1998;84:1346–53. https://doi.org/10.1063/1.368204.
[62] Thornton JA, Hoffman D. Stress-related effects in thin films. Thin Solid Films 1989;171:5–31. https://doi.org/10.1016/0040-6090(89)90030-8.
[63] Ohring M. Mechanical properties of thin films. Materials science of thin films. Academic press; 2001. p. 403–49.
[64] Lu N, Suo Z, Vlassak JJ. The effect of film thickness on the failure strain of polymer-supported metal films. Acta Mater 2010;58:1679–87. https://doi.org/10.1016/j.actamat.2009.11.010.
[65] Leterrier Y, Medico L, Demarco F, Månson J-A, Betz U, Olsson MK, et al. Mechanical integrity of transparent conductive oxide films for flexible polymer-based displays. Thin Solid Films 2004;460:156–66. https://doi.org/10.1016/j.tsf.2004.01.052.
[66] Li T, Huang Z, Xi Z, Lacour SP, Wagner S, Suo Z. Delocalizing strain in a thin metal film on a polymer substrate. Mech Mater 2005;37:261–73. https://doi.org/10.1016/j.mechmat.2004.02.002.
[67] Thompson CV. Solid-state dewetting of thin films. Annu Rev Mater Res 2012;42:399–434. https://doi.org/10.1146/annurev-matsci-070511-155048.
[68] Colla M-S, Amin-Ahmadi B, Idrissi H, Malet L, Godet S, Raskin J-P, et al. Dislocation-mediated relaxation in nanograined columnar palladium films revealed by on-chip time-resolved HRTEM testing. Nat Commun 2015;6. https://doi.org/10.1038/ncomms6922.
[69] Freund L, Jonsdottir F. Instability of a biaxially stressed thin film on a substrate due to material diffusion over its free surface. J Mech Phys Solid 1993;41:1245–64. https://doi.org/10.1016/0022-5096(93)90092-T.
[70] Freund L. The stability of a dislocation threading a strained layer on a substrate. J Appl Mech 1987;54:553–7. https://doi.org/10.1115/1.3173068.
[71] Nix WD. Mechanical properties of thin films. Metallurgical transactions A 1989;20:2217–45. https://doi.org/10.1007/BF02666659.
[72] Dragomir I, Ungár T. The dislocations contrast factors of cubic crystals in the Zener constant range between zero and unity. Powder Diffr 2002;17:104–11. https://doi.org/10.1154/1.1471520.
[73] Borbély A, Dragomir-Cernatescu J, Ribárik G, Ungár T. Computer program ANIZC for the calculation of diffraction contrast factors of dislocations in elastically anisotropic cubic, hexagonal and trigonal crystals. J Appl Crystallogr 2003;36:160–2. https://doi.org/10.1107/S0021889802021581.
[74] Scardi P. Recent advancements in whole powder pattern modelling. Zeitschrift fur Kristallographie Supplements 2008;2008:101–11. https://doi.org/10.1016/j.ijhydene.2016.05.244.